Supporting information for "Scaling laws for mixed-heated stagnant lid convection and application to Europa"

Frédéric Deschamps[1] and Kenny Vilella[2]

[1] Institute of Earth Sciences, Academia Sinica, 128 Academia Road Sec. 2, Nangang, Taipei 11529, Taiwan. [2] JSPS International Research Fellow, Hokkaido University, Sapporo, Japan.

This supporting information provides details on the calculation of radial conductive profiles of temperature and heat flux for a mixed-heated system (section S1 and Table S1), and on the trends predicted by scaling laws for interior temperature and surface heat flux (section S2 and Figures S1 and S2). It further describes the methods used to calculate the ice shell properties (heat flux, interior temperature, and stagnant lid thickness ; section S3 and Figures S3 to S5) and the thermal evolution of this shell (section S4 and Figures S6 and S7). Our modelling is mostly similar to that used in Deschamps (2021). Major differences are the treatments of the interior temperature and stagnant lid thickness.

S1. Temperature and heat flux profiles for stagnant lids in mixed-heated systems

S1.1 Temperature and heat flux profiles in conductive mixed-heated systems

Radial profiles of temperature and heat flux for a purely conductive system with internal heat production may be obtained by integrating the heat equation, which writes

$$\frac{\partial}{\partial z}\left(k\frac{\partial T}{\partial z}\right)+\bar{\rho}H=0 \qquad \text{(S1)}$$

in Cartesian geometry, and

$$\frac{1}{r^2}\frac{\partial}{\partial r}\left(r^2 k\frac{\partial T}{\partial r}\right)+\bar{\rho}H=0 \qquad \text{(S2)}$$

in spherical geometry, where T is the temperature, z (in Eq. S1) the depth, r (in Eq. S2) the radius, k the thermal conductivity, $\bar{\rho}$ the density and H the heating rate per unit of mass. Considering that k, $\bar{\rho}$ and H are constant throughout the system, and taking surface and bottom

temperatures, T_{surf} and T_{bot}, as boundary conditions, integrations of Eqs. (S1) and (S2) lead to the expressions listed in Table S1 for the temperature and heat flux profiles. Note that in Cartesian geometry, D is the thickness of the domain, and in spherical geometry, R and r_c are the total and core radii, $f = r_c/R$ the ratio between these radii, and $D = (R - r_c)$, again, the thickness of the conductive layer. Expressions for radial profiles of heat flux (also listed in Table S1) are obtained by derivating the radial profiles for temperature with respect to either z in Cartesian geometry, or r in spherical geometry. In this later case, one may recall that the heat flux is defined as the opposite of the temperature derivative with respect to radius.

In the case of the outer shells of icy bodies, the bottom temperature is known from the liquidus at the bottom of the ice shell. Instead of using T_{bot} as boundary condition, one may use the surface heat flux, Φ_{surf}. This surface heat flux is given by

$$\Phi_{surf} = k\frac{\Delta T}{D} + \frac{\bar{\rho}HD}{2} \quad \text{(S3)}$$

in Cartesian geometry ($z = 0$), and, noting that $(2 - f - f^2) = (1 - f)(2 + f)$ and $R = D/(1 - f)$, by

$$\Phi_{surf} = k\frac{\Delta T}{D}f + \frac{\bar{\rho}HD}{6}(2 + f)\,, \quad \text{(S4)}$$

in spherical geometry ($r = R$). Temperature profiles then write

$$T(z) = T_{surf} + z\frac{\Phi_{surf}}{k} - \frac{\bar{\rho}Hz^2}{2k}\,, \quad \text{(S5)}$$

in Cartesian geometry, and

$$T(r) = T_{surf} - \frac{\Phi_{surf}}{k}R\left(1 - \frac{R}{r}\right) + \frac{\bar{\rho}HR^2}{6k}\left[2\left(1 - \frac{R}{r}\right) + \left(1 - \frac{r^2}{R^2}\right)\right] \quad \text{(S6)}$$

in spherical geometry.

S1.2 Application to stagnant lids

Depending on whether the bottom temperature, T_{bot}, or the surface heat flux, Φ_{surf}, is known or easier to access, either expressions in Table S1 or Eqs. (S5) and (S6) may be used to describe

temperature profiles within conductive systems or conductive layers. These equations may, in particular be used to infer the thermal profile within the rigid lid that forms at the top of a system animated with stagnant-lid convection (section 3.2), which writes

$$< T >= T_{surf} + z\frac{\Phi_{surf}}{k} - \frac{\bar{\rho}Hz^2}{2k} \quad \text{(S7)}$$

in Cartesian geometry, and

$$< T >= T_{surf} - \frac{\Phi_{surf}}{k} R\left(1 - \frac{R}{r}\right) + \frac{\bar{\rho}HR^2}{6k}\left[2\left(1 - \frac{R}{r}\right) + \left(1 - \frac{r^2}{R^2}\right)\right] \quad \text{(S8)}$$

in spherical geometry. If Φ_{surf} is known, Eqs. (S7) and (S8) can be directly used to determine the temperature profiles within the stagnant lid.

If the thickness of the stagnant lid, d_{lid}, and the temperature at its bottom, T_{lid}, are specified instead of the surface heat flux, expressions given in Table S1 lead to

$$< T >= T_{surf} + \Delta T_{lid}\frac{z}{d_{lid}} + \frac{\rho Hz}{2k}(d_{lid} - z) \quad \text{(S9)}$$

in Cartesian geometry, and

$$< T >= T_{surf} - \Delta T_{lid}\frac{R}{d_{lid}} f_{lid}\left(1 - \frac{R}{r}\right) + \frac{\rho HR^2}{6k}\left[f_{lid}(1 + f_{lid})\left(1 - \frac{R}{r}\right) + \left(1 - \frac{r^2}{R^2}\right)\right] \quad \text{(S10)}$$

in spherical geometry, where $\Delta T_{lid} = \left(T_{lid} - T_{surf}\right)$ is the temperature jump across the stagnant lid, and $f_{lid} = (R - d_{lid})/R = 1 - (1 - f)\, d_{lid}/D$ the ratio between the radius of its base and the total radius. Numerical simulations of stagnant lid convection give easily access to the surface heat flux, while the average temperature at the bottom of the stagnant lid, T_{lid}, is more difficult to estimate. To calculate the temperature profiles within stagnant lids Eqs. (S7) and (S8) are thus handier than Eqs. (S9) and (S10).

Heat flux equations in Table S1 may further be used to estimate the temperature at the bottom of stagnant lids given the surface heat flux and the lid thickness. In this case, heat flux writes

$$\Phi(z) = k\frac{\Delta T_{lid}}{d_{lid}} + \frac{\bar{\rho}H}{2}(d_{lid} - 2z) \quad \text{(S11)}$$

in Cartesian geometry, and

$$\Phi(r) = k\frac{\Delta T_{lid}}{d_{lid}} f_{lid}\left(\frac{R}{r}\right)^2 + \frac{\bar{\rho}Hr}{3}\left[1 - \frac{f_{lid}(1+f_{lid})}{2}\frac{R^3}{r^3}\right] \quad \text{(S12)}$$

in spherical geometry. Taking Eqs. (S11) and (S12) at the surface (z = 0 or r = R), and rearranging the terms, one gets the temperature at the bottom of the lid, $T_{lid} = T_{surf} + \Delta T_{lid}$, as a function of the surface heat flux and stagnant lid thickness, following

$$T_{lid} = T_{surf} + \frac{d_{lid}}{k}\left(\Phi_{surf} - \frac{\bar{\rho}Hd_{lid}}{2}\right) \quad \text{(S13)}$$

in Cartesian geometry, and

$$T_{lid} = T_{surf} + \frac{d_{lid}}{kf_{lid}}\left[\Phi_{surf} - \frac{\bar{\rho}HR}{6}(2 - f_{lid} - f_{lid}^2)\right] \quad \text{(S14)}$$

in spherical geometry.

S2. Trends in scaling laws for temperature and heat flux

Supplementary Figures S1 and S2 plot the non-dimensional interior temperature, $\tilde{T}_m$, and surface heat flux, $\widetilde{\Phi}_{top}$, as a function of the input parameters of numerical simulations and following scaling laws inferred in sections 4.1 and 4.2 of the main article (Eqs. 21 and 23). Input parameters are the surface Rayleigh number, Ra_{surf}, the ratio between the inner and outer radii of the shell, f (with f = 1 for Cartesian geometry), the non-dimensional rate of internal heating, $\widetilde{H}$, and the non-dimensional inverse of the viscous temperature scale, γ, controlling the amplitude of viscosity variations with temperature. The viscosity law follows the Frank-Kamenetskii approximation, implying that $\gamma = \ln(\Delta\eta)$, where $\Delta\eta$ is the top-to-bottom viscosity ratio. As discussed in sections 4.1 and 4.2, two sets of parameters are needed to explain the results of the simulations, depending on whether the Urey number, Ur, defined by Eq. (12) of the main text, is smaller or larger than 1. This leads to discontinuities for cases where $Ur \sim 1$.

Figure S1 shows that $\tilde{T}_m$ increases with $\tilde{H}$, as one would expect, but decreases with increasing Ra_{surf}, while $\tilde{\Phi}_{top}$ increases monotically with both $\tilde{H}$ and Ra_{surf}. Interior temperature further decreases as curvature gets larger (*f* decreases). The amplitude of variations in $\tilde{T}_m$ with *f* are rather limited compared to variations of $\tilde{T}_m$ with $\tilde{H}$, but comparable to those induced by changes in Ra_{surf}. Note that $\tilde{\Phi}_{top}$ does not depend explicitly on *f* (Eq. 23 of main text), but is nevertheless sensitive to this parameter because the effective Rayleigh number, Ra_{eff} (Eq. 10 of main article) depends on temperature. As a consequence, $\tilde{\Phi}_{top}$ decreases with increasing curvature, but these variations are relatively limited compared to those induced by changes in Ra_{surf} or $\tilde{H}$.

The influence of γ on $\tilde{T}_m$ is more complex and depends in particular on the value of $\tilde{H}$ (plots a and b in Figure S2). For $\tilde{H} < 1$, $\tilde{T}_m$ monotically increases with γ (and thus with Δη), as observed for stagnant-lid convection with a bottom heated-fluid, i.e., $\tilde{H} = 0$ (*e.g.*, Moresi and Solomatov, 1995; Deschamps and Sotin, 2000). By contrast, for $\tilde{H}$ around 1 and higher, $\tilde{T}_m$ first decreases with increasing γ, reaches a minimum value for a value of γ that increases with $\tilde{H}$, and starts increasing again. It is also interesting to note that the influence of $\tilde{H}$ becomes smaller as γ increases, *i.e.*, for high values of γ (typically, larger than 25-30), $\tilde{T}_m$ is mostly controlled by γ (and thus by the thermal viscosity contrast) regardless of $\tilde{H}$. As a consequence, $\tilde{T}_m < 1$ (and thus *Ur* < 1) for such values of γ, and $\tilde{T}_m$ tends asymptotically to 1 as γ goes to infinity. Finally, plots c and d in Figure S2 indicate that $\tilde{\Phi}_{top}$ increases monotically with γ. As discussed in section 4.2, γ acts on $\tilde{\Phi}_{top}$ directly, through $1/\gamma^c$ and the exponential term defining Ra_{eff}, and indirectly through $\tilde{T}_m$. Both the $1/\gamma^c$ term in Eq. (23) and, if γ is not too large, the decrease in $\tilde{T}_m$ (and thus in Ra_{eff}) lead to a decrease in $\tilde{\Phi}_{top}$ as Δη gets larger. However, the exponential term in the definition of Ra_{eff} is dominant, such that for given values of Ra_{surf} and $\tilde{H}$, $\tilde{\Phi}_{top}$ increases with Δη. Again, it is worth noting that the influence of $\tilde{H}$ diminishes as γ

gets larger, and that for high viscosity ratios the value of $\widetilde{\Phi}_{top}$ is mostly controlled by the amplitude of these variations.

S3. Modelling of ice shell properties

For applications to Europa, we assumed that the viscosity of ice Ih is described by

$$\eta(T) = \eta_{ref} exp\left[\frac{E}{RT_{ref}}\left(\frac{T_{ref}}{T} - 1\right)\right] \quad \text{(S15)}$$

where E is the activation energy, R the ideal gas constant, and η_{ref} the reference viscosity at temperature T_{ref}. The reference viscosity is not well constrained. Close to the melting point, *i.e.* for T_{ref} equal to the liquidus temperature of pure water at the bottom of the ice shell, $T_{H2O,bot}$, a range of values based on polar ice sheet creep is 10^{13}-10^{15} Pa s (Montagnat and Duval, 2000). Here, we considered this parameter as a free parameter and varied it in the range 10^{12}-10^{15} Pa s, extending the range of possible values estimated by Montagnat and Duval (2000). Activation energy is better constrained, with values in the range 49-60 kJ/mol depending on the creep regime (Durham et al., 2010), and around 60 kJ/mol for atomic diffusion (Weertman, 1983). Here, we used E = 60 kJ/mol in all calculations. Under icy moons conditions, ice Ih rheology is likely more complex than the diffusion creep mechanism assumed in Eq. (S15), but it is reasonable to think that the impact of internal heating on ice shell dynamics follows a similar trend for different rheologies.

Following Eq. (22) and the viscosity law (Eq. S15), the viscous temperature scale is

$$\Delta T_v = \frac{RT_m{}^2}{E}, \quad \text{(S16)}$$

such that the inverse of the non-dimensional viscous temperature scale, $\gamma = \Delta T/\Delta T_v$, which controls the thermal viscosity contrast, is given by

$$\gamma = \frac{E\Delta T}{RT_m{}^2}, \quad \text{(S17)}$$

where $\Delta T = \left(T_{bot} - T_{surf}\right)$ is the top to bottom temperature jump. Still following Eq. (S16), rescaling Eq. (21) of main text gives the interior temperature

$$T_m = T_{bot} - \frac{a_1 R}{E f^{a_2}} {T_m}^2 + (a_1 + a_2 f)\left[\frac{\left(1+f+f^2\right)}{3}\frac{\rho_I H D^2}{k_I \Delta T}\right]^{c_3} \frac{\Delta T}{{Ra_{eff}}^{c_4}}, \quad \text{(S18)}$$

where T_{bot} is the bottom temperature defined as the liquidus of the water + impurities system, H the internal heating rate per mass unit, ρ_I and k_I the density and thermal conductivity of the ice Ih, respectively, D the thickness of the ice layer, and Ra_{eff} the Rayleigh number calculated with the viscosity temperature T_m,

$$Ra_{eff} = \frac{\alpha_I \rho_I g \Delta T D^3}{\eta(T_m)\kappa_I}, \quad \text{(S19)}$$

In Eq. (S19), α_I and κ_I are the thermal expansion and thermal diffusivity of ice Ih, and $\eta(T_m)$ is calculated with Eq. (S15). The values of the parameters a_1, a_2, and c_1 to c_4 are given in section 4.1. Note that parameters c_1 to c_4 have different values depending on whether the Urey ratio (Ur, Eq. 12 of main text) is smaller or larger than 1. It is also worth noting that if the sub-surface ocean is composed of pure water, the bottom temperature T_{bot} is equal to the reference temperature defined in the viscosity law (Eq. S15), but is lower than this reference temperature if impurities (*e.g.*, ammonia) are also present (see next paragraph). Equation (S18) does not have analytical solution, and we solved it following a Newton-Raphson zero-search method.

Impurities act as an anti-freeze and may include ammonia (NH_3), methanol (CH_3OH), and salts (*e.g.*, magnesium sulfate, $MgSO_4$). Here, we more specifically considered ammonia, which is predicted to condensate in giant planets environments with amounts up to a few per cent (Mousis et al., 2009; Deschamps et al., 2010). In the case of Europa, magnesium sulfate may further be an important compound of the ocean (Vance et al. 2018). Qualitatively, however, the evolution of the icy bodies is not significantly impacted by the nature of the impurities, but only by their amount. For instance, Vilella et al. (2020) pointed out that the impact of 30 % $MgSO_4$ on the liquidus is equivalent to that of 3.5 % NH_3. On another hand, it should be noted

that different compositions may impact physical properties of the ocean, in particular its density. Adding 30 % $MgSO_4$ would increase density by about 150 kg/m^3, while 3.5 % NH_3 would reduce it. Details on the calculation of the water-ammonia system liquidus can be found in Deschamps and Sotin (2001). Practically, we prescribed the initial fraction of ammonia, corresponding to the concentration of ammonia in the initial ocean. The concentration in ammonia then increases as the ocean starts to freeze, since up to the eutectic composition (equal to 32.2 wt% in the case of NH_3), only water ice crystalizes, while impurities are left in the subsurface ocean, whose volume decreases due to the thickening of the outer ice layer. Note that in phase diagrams, concentrations in impurities are usually measured in wt%. For practical reasons, we perform calculations with the volume fraction, which we correct to weight fraction when determining the liquidus, following (in the case of ammonia)

$$x_{NH3}^{wt} = \frac{x_{NH3}^{vol}\rho_{NH3}}{x_{NH3}^{vol}\rho_{NH3} + (1-x_{NH3}^{vol})\rho_w}, \quad \text{(S20)}$$

where ρ_w and ρ_{NH3} are the densities of liquid water and ammonia, respectively.

The surface heat flux is obtained by rescaling the heat flux scaling law (Eq. 23 of main text) with the characteristic heat flux, $\Phi_{carac} = k_{ref}\,\Delta T/D$, where k_{ref} is the characteristic thermal conductivity. Most reconstruction of icy bodies thermal evolutions used values of k_{ref} in the range 2.0-3.0 W/m/K, corresponding to the conductivity at the temperature of the well mixed interior or at the bottom of the shell (*e.g.*, Grasset et al., 1996; Tobie et al., 2003; Běhounková et al., 2010). Here, we fixed k_{ref} to 2.6 W/m/K (Grasset and Sotin, 1996). Interestingly, in the case of Europa, this value leads to ice shell properties and thermal evolution very close to those obtained with temperature-dependent thermal conductivity (Deschamps, 2021). Accounting for the shell's curvature, measured with the ratio between the inner and outer radii, *f*, the basal and surface heat fluxes write

$$\Phi_{surf} = \Phi_{carac}\widetilde{\Phi}_{top} \quad \text{(S21)}$$

and $$\Phi_{bot} = \Phi_{carac}\widetilde{\Phi}_{top}/f^2\,. \quad \text{(S22)}$$

Note that this formulation is slightly different from that used in Deschamps (2021), where the non-dimensional convective heat flux ($\widetilde{\Phi}_{conv}$) was inferred from 3D-Cartesian calculations and a correction for spherical geometry was assumed, leading to $\Phi_{surf} = f\Phi_{carac}\widetilde{\Phi}_{conv}$ and $\Phi_{bot} = \Phi_{carac}\widetilde{\Phi}_{conv}/f$. Because the curvature of outer ice layers of large icy bodies remains large (typically, f > 0.7), this difference only triggers small to moderate effects on the calculations of ice shell properties and thermal evolution. Note that if the surface heat flux is lower than the conductive characteristic heat flux, Φ_{carac}, the system is not animated by convection and transfers heat by conduction. This occurs, for instance, if the ice shell is too thin or, in the case of a sub-surface ocean containing impurities, too thick. In this later case, the temperature at the bottom of the shell is much lower than in the case of a pure water ocean. As a result, reference and interior viscosities are higher, decreasing the vigor of convection or even shutting off convection (Deschamps and Sotin, 2001).

As discussed in main text, two sets of parameters for Eq. (23) may be used, depending on whether the bottom heat flux, Φ_{bot}, is positive (Ur < 1) or negative (Ur > 1). The threshold (non-dimensional) internal heating is given by Eq. (25) of main text, and may be used as a criteria to decide which set of parameters to use. Here, instead, we used a simpler procedure, which accounts for the fact that temperature and heat flux scalings are not continuous at Ur = 1. First, we calculate the internal temperature T_m (Eq. S18) and the surface heat flux, Φ_{surf}, assuming parameter values for Ur < 1. If the corresponding Φ_{bot} (calculated with Eq. (11) of main text) is negative, we re-evaluate T_m and Φ_{surf}, but with parameter values for Ur > 1. If the resulting Φ_{bot} is positive again, we set arbitrarily its value to zero, and recalculate Φ_{surf} and T_m accordingly.

To calculate the thickness of the stagnant lid, Deschamps (2021) assumed that the temperature at the bottom of the lid is well described by $T_{lid} = 2T_m - T_{bot}$, and then deduced d_{lid} from the expression of the conductive temperature profile within the lid. However, the

relationship between T_{lid} and T_m assumes that temperature jump in the bottom and top thermal boundary layers (excluding the stagnant lid) are equal, which is not valid for mixed-heating convection. Here, instead, we estimated the thickness of the stagnant lid by rescaling Eq. (26) of the main article, leading to

$$d_{lid} = \frac{a_{lid}\gamma^c}{Ra_{eff}{}^b} D \ , \quad \text{(S23)}$$

where γ and Ra_{eff} are given by Eqs. (S17) and (S19), respectively, the constant a_{lid} is equal to 0.633 for $Ur < 1$ and 0.667 for $Ur > 1$, $b = 0.27$, and $c = 1.21$. The temperature at the bottom of the stagnant lid can then be calculated using Eq. (S14).

S4. Thermal evolution

The present day radial structure of icy bodies may be estimated from appropriate thermal evolution modelling. Here, we followed the approach of Grasset and Sotin (1996), which calculates the evolution of ice layers thicknesses based on an energy balance accounting for the production of heat in the silicate core, the cooling of the ocean, and the crystallization of ice shells. Europa is not large enough to host high pressure ices, such that the inner radius of the outer ice Ih shell, r_{bot}, can be calculated by solving the energy conservation equation at the boundary between this shell and the sub-surface ocean. Energy conservation at this boundary then writes

$$\frac{dr_{bot}}{dt}\left[\rho_w C_w \left(-\frac{\partial T_{ad}}{\partial r} + \frac{\partial T_{bot}}{\partial r}\right)\frac{\left(r_{bot}{}^3 - r_c{}^3\right)}{3} - \rho_I L_I r_{bot}{}^2\right] = r_{bot}{}^2 \Phi_{bot} - r_c{}^2 \Phi_c \quad \text{(S24)}$$

where t is time, T_{bot} and Φ_{bot} are the temperature and heat flux at the bottom of the ice layer, given by the liquidus of the ocean and by Eq. (S22), respectively, r_c is the core radius, Φ_c the heat flux at the top of the core, ρ_w and C_w the liquid water density and heat capacity, ρ_I and L_I the density and latent heat of fusion of ice Ih, respectively, and T_{ad}, the adiabatic temperature in the ocean, given by

$$T_{ad}(r) = T_{bot}(r_{bot})\left[1 - \frac{\alpha_w}{\rho_w C_w}\rho_I g(r - r_{bot})\right], \quad \text{(S25)}$$

with α_w being the thermal expansion of liquid water. Within the silicate core, heat is assumed to be produced by the decay of 4 radiogenic elements, ^{40}K, ^{232}Th, ^{235}U, and ^{238}U. The heat flux at the top of the core is then calculated following Kirk and Stevenson (1987) by

$$\Phi_c = 2\sqrt{\frac{\kappa_c t}{\pi}}\rho_c \sum_{i=1}^{4} C_{0,i} H_i \frac{[1-\exp(-\lambda_i t)]}{\lambda_i t}, \quad \text{(S26)}$$

where κ_c and ρ_c are the thermal diffusivity and density of the silicate core, and the subscript *i* refers to the 4 radiogenic elements, whose properties are listed in Table S2. We solved Eq. (S24) up to t = 4.55 Gyr using an adaptative stepsize control Runge-Kutta method (Press et al., 1992), and assuming an initial ice Ih thickness equal to 10 km together with the material and physical properties listed in Table 3 of the main text. Again, because the reference viscosity η_{ref} is a sensitive parameter but is poorly constrained, we performed calculations for values of η_{ref} in the range 10^{12}-10^{15} Pa s, corresponding to an extended range of the values estimated by Montagnat and Duval (2000).

References

Běhounková, M., Tobie, G., Choblet, G., & Čadek, O. (2010). Coupling mantle convection and tidal dissipation : Applications to Enceladus and terrestrial planets, *J. Geophys. Res. Planets*, *115*, doi: 10.1029/2009JE003564.

Davaille, A., & Jaupart, C. (1993). Transient high-Rayleigh-number thermal convection with large viscosity variations. *J. Fluid Mech.*, *253*, 141-166.

Deschamps, F. (2021). Stagnant lid convection with temperature-dependent thermal conductivity and the thermal evolution of icy worlds, *Geophys. J. Int.*, *224*, 1870-1890.

Deschamps, F., & Sotin, C. (2000). Inversion of two-dimensional numerical convection experiments for a fluid with a strongly temperature-dependent viscosity. *Geophys. J. Int.*, *143*, 204-218.

Deschamps, F. & Sotin, C. (2001). Thermal convection in the outer shell of large icy satellites, *J. Geophys. Res.*, *106*, 5107-5121.

Deschamps, F., Mousis, O., Sanchez-Valle, C. & Lunine, J.I. (2010). The role of methanol on the crystallization of Titan's primordial ocean. *Astrophys. J.*, *724*, 887-894.

Durham, W.B., Prieto-Ballesteros, O., Goldsby, D.L. & Kargel, J.S. (2010). Rheological and thermal properties of icy minerals, *Space Sci. Rev.*, *153*, 273-298.

Grasset, O. & Sotin, C. (1996). The cooling rate of a liquid shell in Titan's interior, *Icarus*, *123*, 101-112.

Kirk, R.L. & Stevenson, D.J. (1987). Thermal evolution of a differentiated Ganymede and implications for surface features, *Icarus*, *69*, 91-134.

Montagnat, M. & Duval, P. (2000). Rate controlling processes in the creep of polar ice, influence of grain boundary migration associated with recrystallization, *Earth Planet. Sci. Lett.*, *183*, 179-186.

Moresi, L.-N. & Solomatov, V.S. (1995). Numerical investigation of 2D convection with extremely large viscosity variations, *Phys. Fluids*, **7**, 2154-2162.

Mousis, O., Lunine, J. I., Thomas, C., Pasek, M., Marboeuf, U., Alibert, Y., Ballenegger, V., Cordier, D., Ellinger, Y., Pauzat, F., & Picaud, S. (2009). Clathration of volatiles in the Solar nebula and implications for the origin of Titan's atmosphere. *The Astrophysical Journal*, *691*, 1780-1786.

Press, W.H., Flannery, B.P. Teukolsky, S.A. & Vetterling, W.T. (1992). Numerical Recipes, 2nd edtion, Cambridge University Press, pp. 701-725.

290 Tobie, G., Choblet, G. & Sotin, C. (2003). Tidally heated convection: constraints on Europa's
291 ice shell thickness, *J. Geophys. Res.*, *108*, doi: 10.1029/2003JE002099.
292 Vilella, K., Choblet, G., Tsao, W.E. & Deschamps, F. (2020). Tidally heated convection and
293 the occurrence of melting in icy satellites: application to Europa, *J. Geophys. Res. Planets*,
294 *125*, e2019JE006248, doi: 10.1029/2019JE006248.
295 Weertman, J. (1983). Creep deformation of ice, *Ann. Rev. Earth Planet. Sci.*, *11*, 215-240.
296

Table S1. Relationships for radial profiles of temperature and heat flux for a conductive mixed-heated system.

Quantity	Geometry	Expression
Temperature	Cartesian	$T_{surf} + \Delta T \frac{z}{D} + \frac{\bar{\rho} H z}{2k}(D - z)$
-	Spherical	$T_{surf} - \Delta T \frac{R}{D} f\left(1 - \frac{R}{r}\right) + \frac{\bar{\rho} H R^2}{6k}\left[f(1+f)\left(1 - \frac{R}{r}\right) + \left(1 - \frac{r^2}{R^2}\right)\right]$
Heat flux	Cartesian	$k\frac{\Delta T}{D} + \frac{\bar{\rho} H}{2}(D - 2z)$
-	Spherical	$k\frac{\Delta T}{D} f\left(\frac{R}{r}\right)^2 + \frac{\bar{\rho} H r}{3}\left[1 - \frac{f(1+f)}{2}\frac{R^3}{r^3}\right]$

ΔT = (T_{bot} - T_{surf}) is the bottom-to-top temperature jump, where T_{surf} and T_{bot} are the surface and bottom temperature and D is the thickness of the shell. In Cartesian geometry, z is depth, and in spherical geometry, r is radius, R the total radius, and $f = r_{bot}/R$ the ratio between the inner and outer radii of the shell. k is the thermal conductivity, H the rate of internal heating, and $\bar{\rho}$ the average density, which are here all considered as being constant.

Table S2. Properties of long-lived radioactive isotopes.

Element	Decay constant, λ (1/yr)	Heat release, H (W/kg)	Initial abundance, C_0 (ppb)
^{40}K	5.4279×10^{-10}	2.917×10^{-5}	738.0
^{232}Th	4.9405×10^{-11}	2.638×10^{-5}	38.7
^{235}U	9.8485×10^{-10}	5.687×10^{-4}	5.4
^{238}U	1.5514×10^{-10}	9.465×10^{-5}	19.9

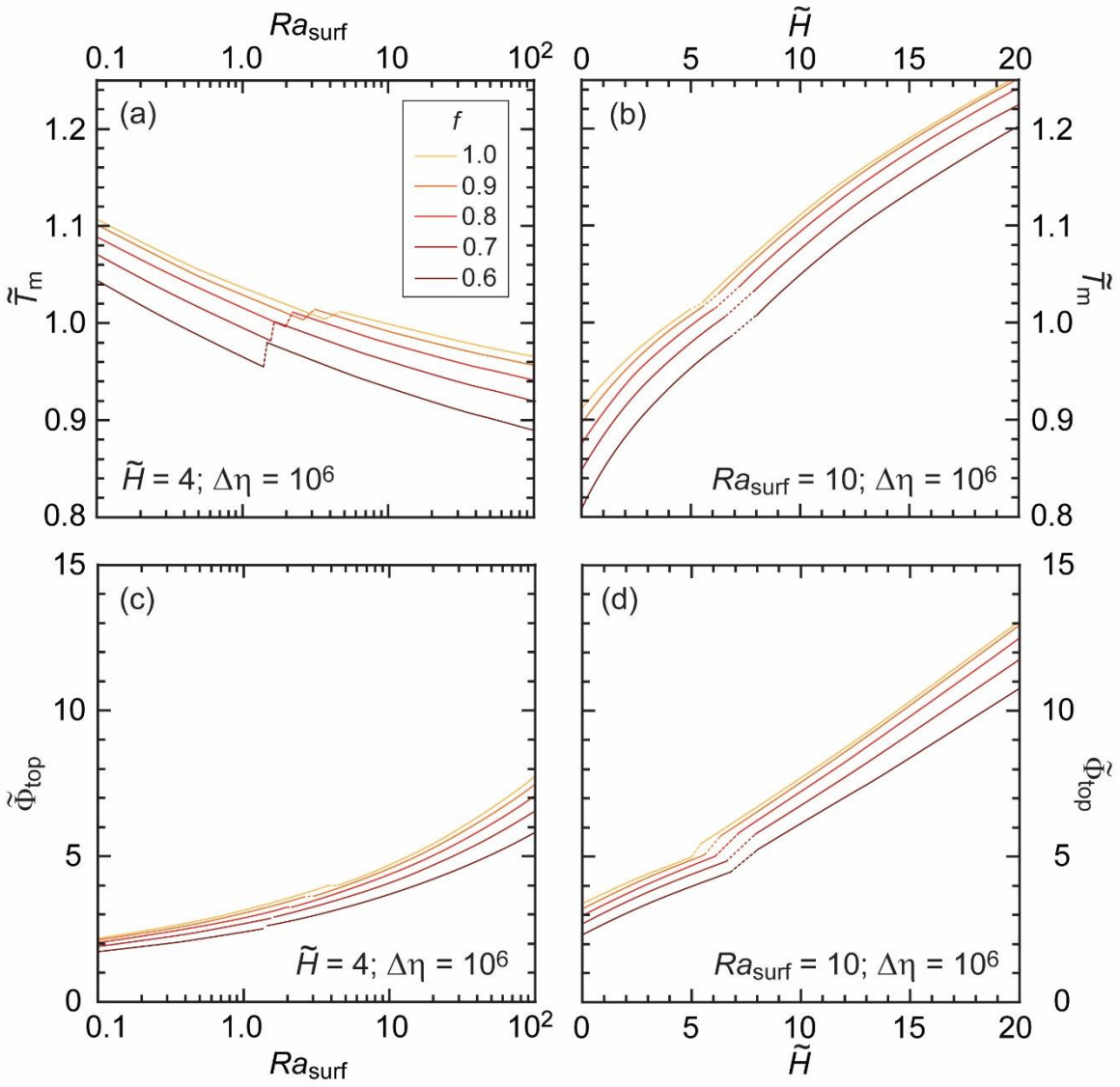

Figure S1. Non-dimensional interior temperature $\tilde{T}_m$ deduced from Eq. (21) (top row) and surface heat flux $\tilde{\Phi}_{top}$ calculated from Eq. (23) (bottom row) as a function of the surface Rayleigh number Ra_{surf} (left column) and non-dimensional rate of internal heating $\tilde{H}$ (right column), and for several values of the ratio between the inner and outer shell radii f (color code; f = 1 indicates Cartesian geometry). Two sets of parameters for Eqs. (21) and (23) are used, depending on whether the Urey ratio (*Ur*, Eq. 12) is smaller or larger than 1 (see main article), leading to discontinuities at $Ur \sim 1$. For calculations as a function of Ra_{surf} (left column), $\tilde{H}$ is set to 4, and for calculations as a function of $\tilde{H}$ (right column), Ra_{surf} is equal to 10. In all cases, the surface top-to-bottom viscosity ratio is fixed to 10^6.

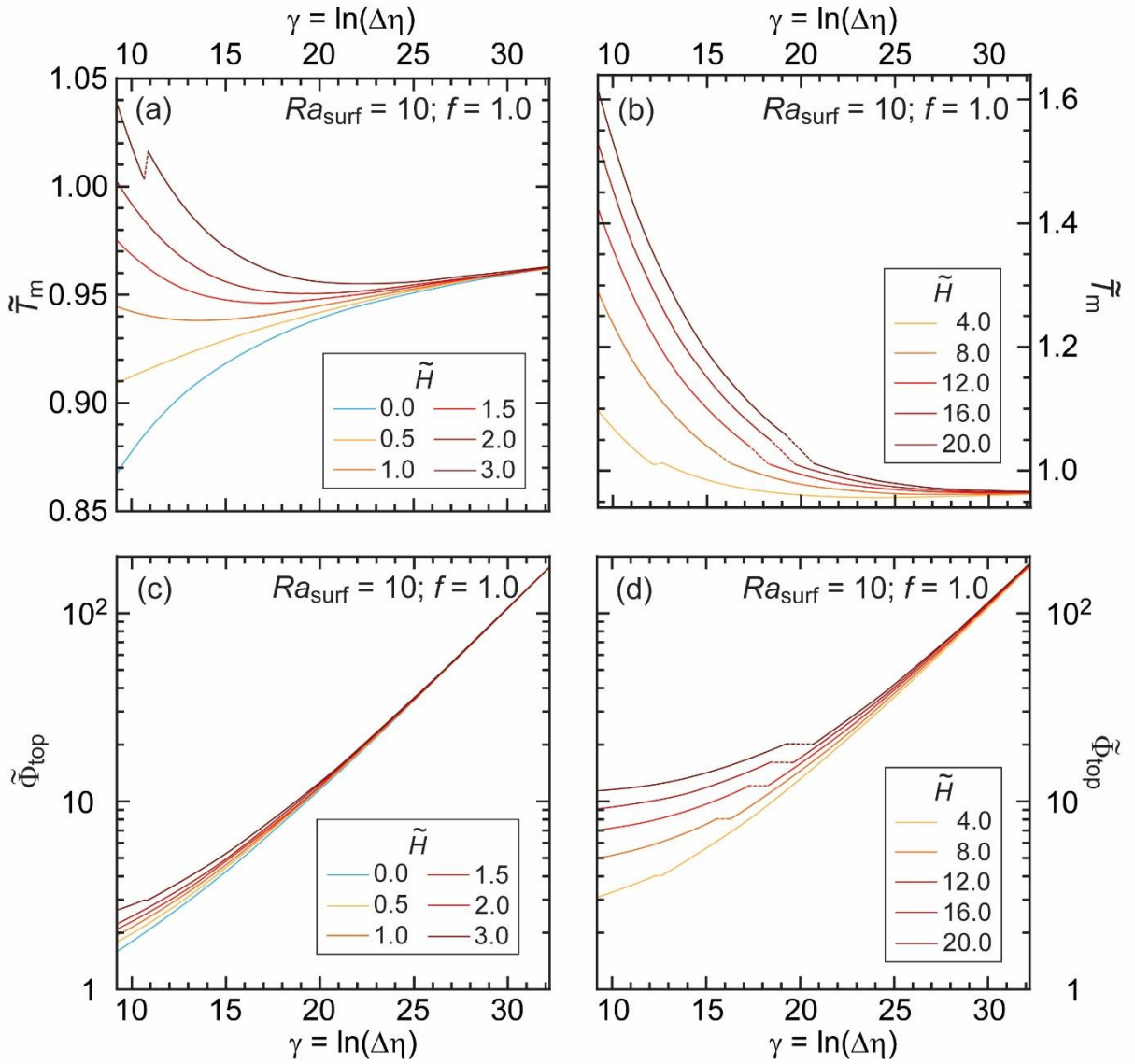

Figure S2. Non-dimensional interior temperature $\tilde{T}_m$ deduced from Eq. (21) (top row) and surface heat flux $\tilde{\Phi}_{top}$ calculated from Eq. (23) (bottom row) as a function inverse of the non-dimensional viscous temperature scale, $\gamma = \Delta T / \Delta T_v$ (see main text), and for several values of the non-dimensional rate of internal heating (color code). The viscosity is described by a Frank-Kamenetskii law (Eq. 7), such that γ is equal to the logarithm of the top-to-bottom viscosity ratio. Two sets of parameters for Eqs. (21) and (23) are used, depending on whether the Urey ratio (*Ur*, Eq. 12) is smaller or larger than 1 (see main article) and leading to discontinuities at *Ur* ~ 1. In all cases, the surface Rayleigh number is equal to 10, and geometry is Cartesian (*f* = 1).

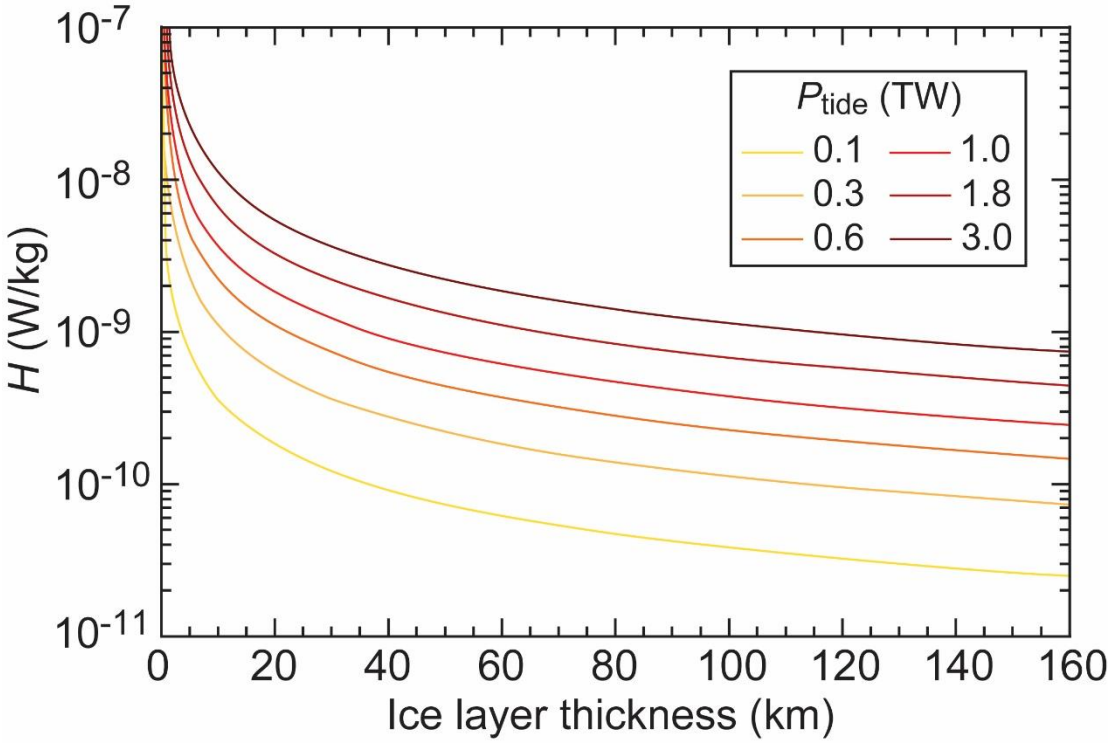

Figure S3. Rate of internal heating per mass unit as a function of the ice shell thickness and for several values of the total power dissipated in the ice layer (color code). The density of the ice shell is ρ_I = 920 kg/m^3.

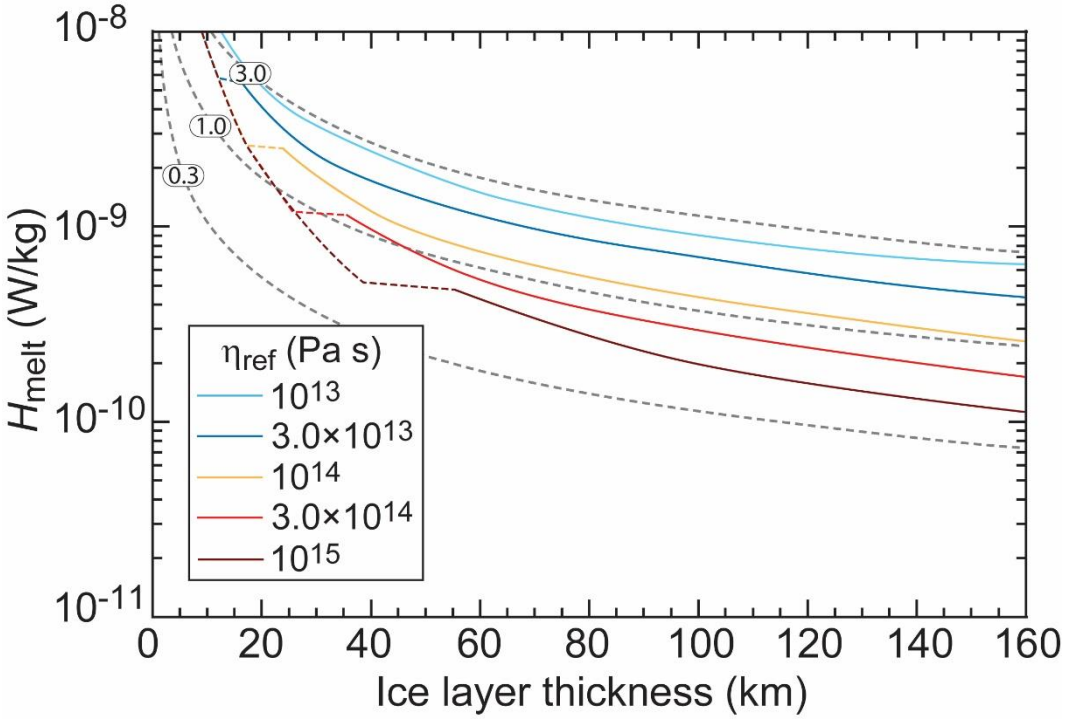

Figure S4. Critical values of internal heating for partial melting of the ice shell, H_{melt}, as a function of the ice shell thickness and for different values of the reference viscosity, η_{ref}. Calculations are made with the properties of Europa (Table 3) and assuming a sub-surface ocean composed of pure water. Dashed parts of the curves indicate that the system is not animated by convection, based on the observation that the convective heat flux is smaller than the conductive heat flux. The grey dashed curves represent the heating rate for three values of the total power dissipated within the ice shell (values in TW indicated on each curve).

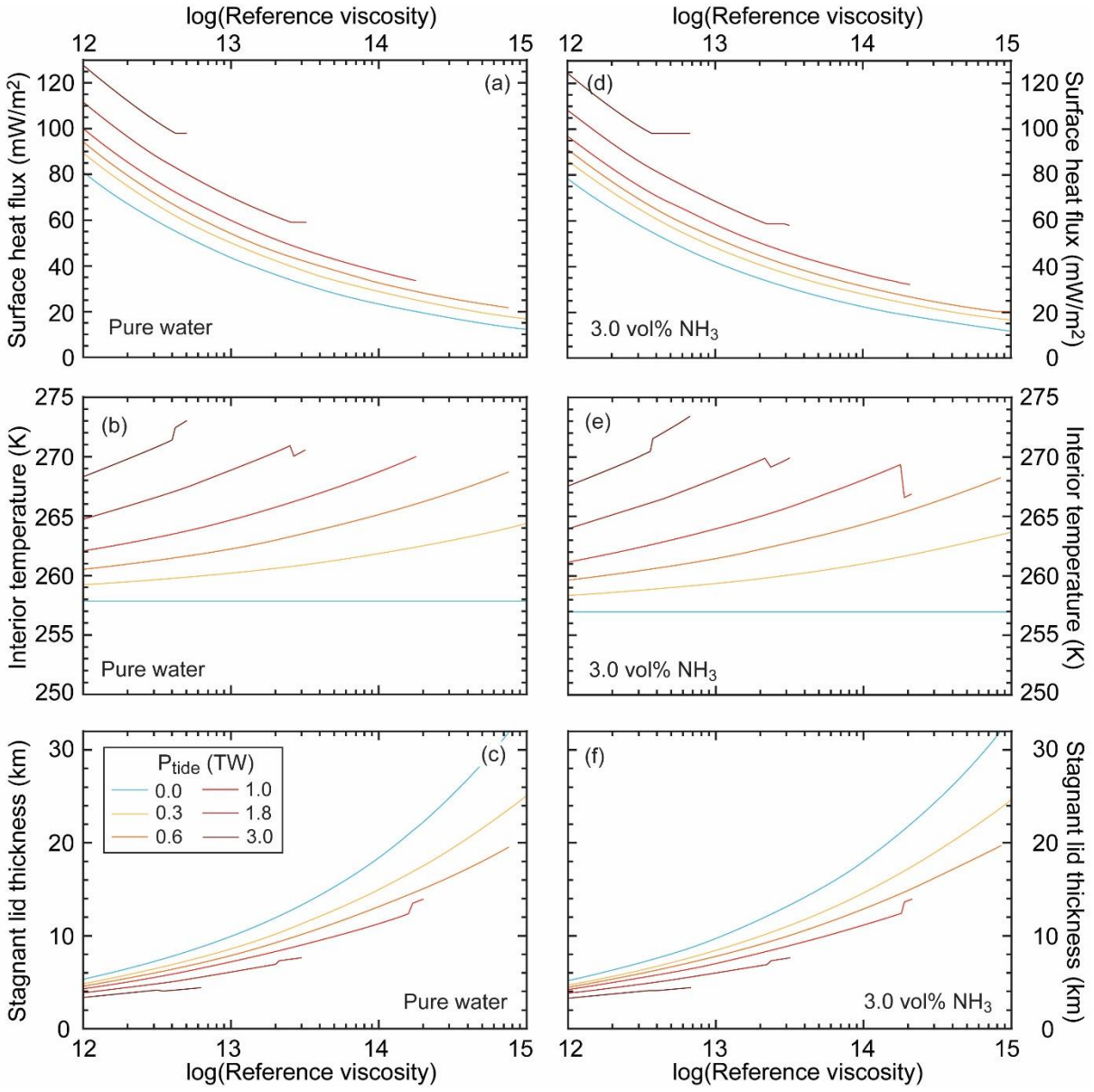

Figure S5. Properties of a 40 km thick ice Ih shell as a function of the reference viscosity, η_{ref}, and for several values of the total power dissipated in the ice layer (color code). (a) and (d) Surface heat flux. (b) and (e) Interior temperature. (c) and (f) Stagnant lid thickness. Physical properties used for calculations are listed in Table 3, and two initial compositions of the ocean are considered, pure water (left column), and an initial mix of water and 3.0 vol% ammonia (right column). Curves interruptions indicate that the average interior temperature is larger than the liquidus of pure water at that depth. Two regimes occur depending on whether the Urey ratio (*Ur*, Eq. 12) is smaller or larger than 1, leading to discontinuities at $Ur \sim 1$.

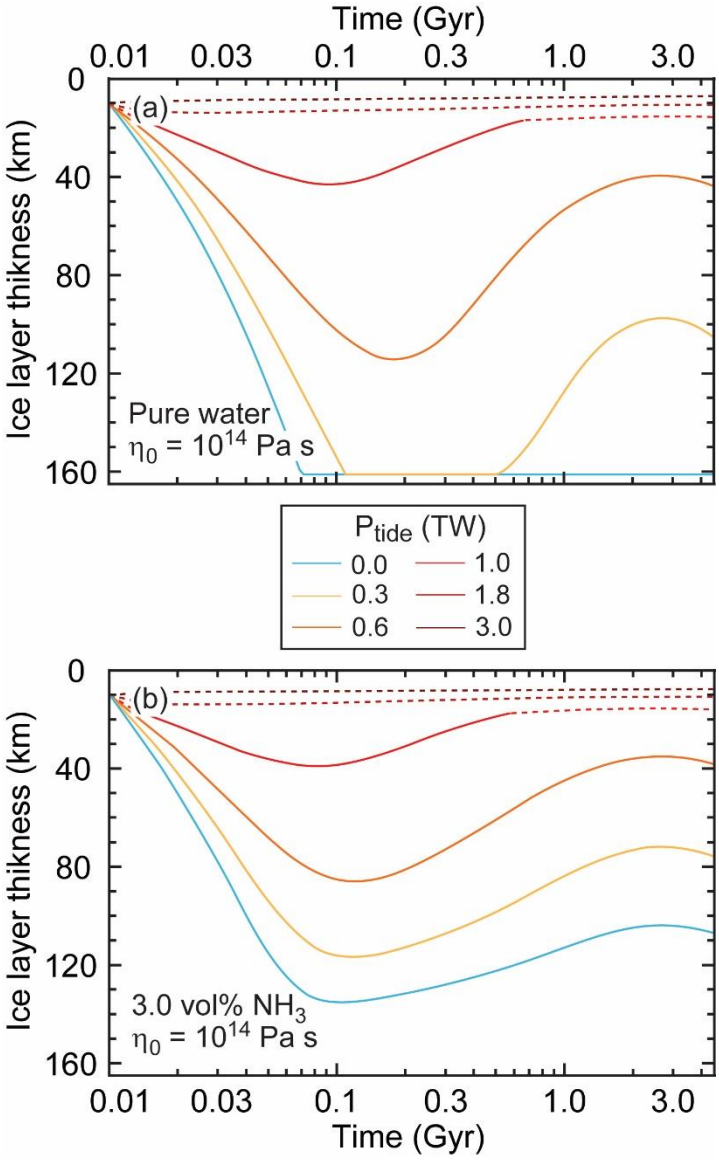

Figure S6. Evolution of the ice shell thickness as a function of time for reference viscosity η_{ref} = 10^{14} Pa s and several values of the total power dissipated in the ice layer (color code). The composition of the ocean is (a) pure water, or (b) an initial mix of water and 3.0 vol% ammonia. Note the logarithmic scale for the time axis.

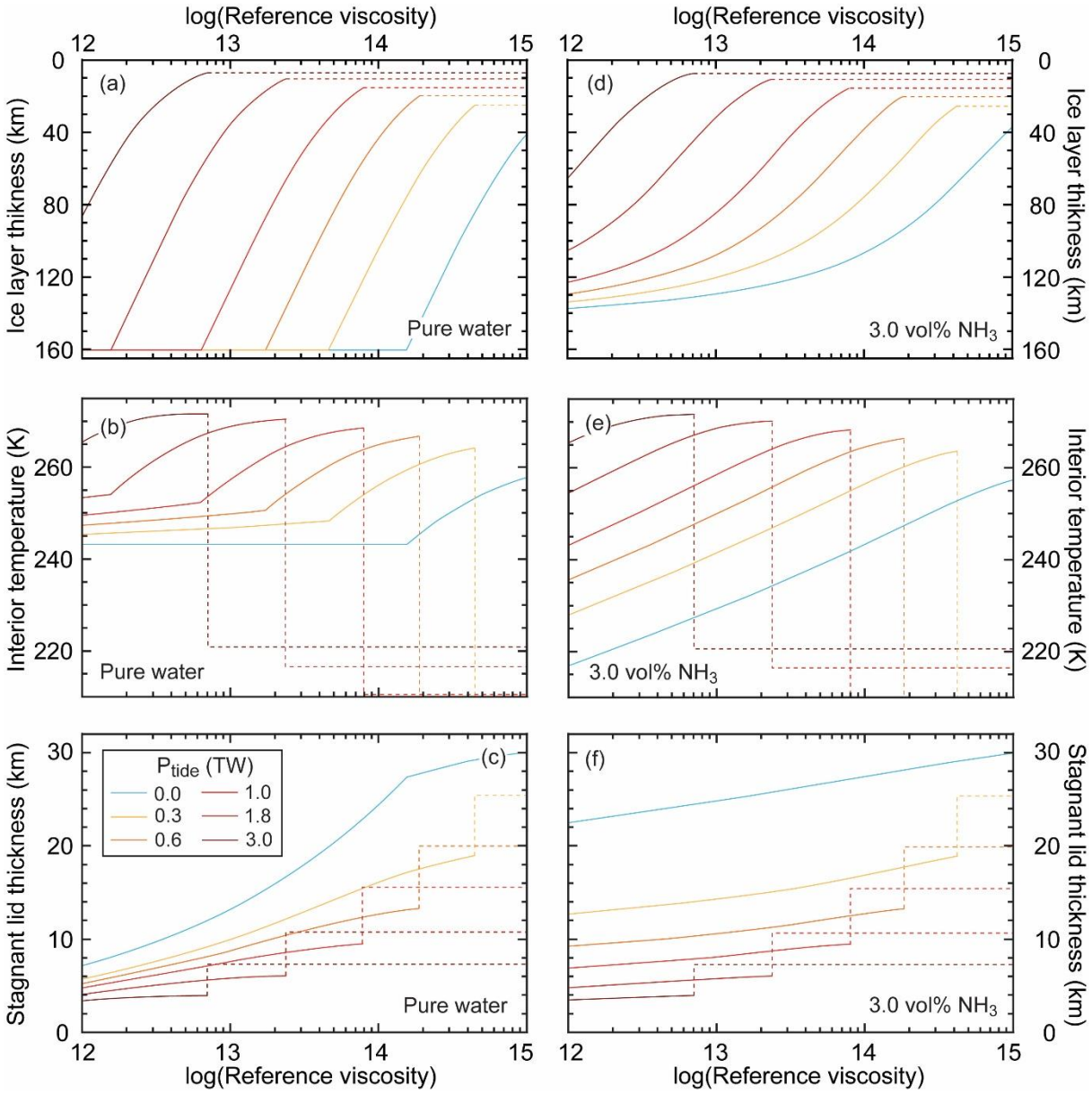

Figure S7. Properties of Europa's outer ice shell at t = 4.55 Gyr as a function of the reference viscosity, η_{ref}, and for several values of the total power dissipated in the ice layer (color code). (a) and (d) Ice shell thickness. (b) and (e) Interior temperature. (c) and (f) Stagnant lid thickness. Physical properties used for calculations are listed in Table 3, and two initial compositions of the ocean are considered, pure water (left column), and an initial mix of water and 3.0 vol% ammonia (right column). Dashed parts of the curves indicate that the system is not animated by convection.